Biomechanics and Modeling in Mechanobiology
https://doi.org/10.1007/s10237-024-01897-5

ORIGINAL PAPER

A multiphasic model for determination of mouse ascending thoracic aorta mass transport properties with and without aneurysm

Keshav A. Kailash[1] · Shamimur R. Akanda[1] · Alexandra L. Davis[1] · Christie L. Crandall[3] · Luis A. Castro[3] · Lori A. Setton[1,2,3] · Jessica E. Wagenseil[3]

Received: 8 May 2024 / Accepted: 10 October 2024

Abstract
Thoracic aortic aneurysms (TAAs) are associated with aortic wall remodeling that affects transmural transport or the movement of fluid and solute across the wall. In previous work, we used a $Fbln4^{E57K/E57K}$ (MU) mouse model to investigate transmural transport changes as a function of aneurysm severity. We compared wild-type (WT), MU with no aneurysm (MU-NA), MU with aneurysm (MU-A), and MU with an additional genetic mutation that led to increased aneurysm penetrance (MU-XA). We found that all aneurysmal aortas (MU-A and MU-XA) had lower fluid flux compared to WT. Non-aneurysmal aortas (MU-NA) had higher 4 kDa FITC-dextran solute flux than WT, but aneurysmal MU-A and MU-XA aortas had solute fluxes similar to WT. Our experimental results could not isolate competing factors, such as changes in aortic geometry and solid material properties among these mouse models, to determine how intrinsic transport properties change with aneurysm severity. The objective of this study is to use biphasic and multiphasic models to identify changes in transport material properties. Our biphasic model indicates that hydraulic permeability is significantly decreased in the severe aneurysm model (MU-XA) compared to non-aneurysmal aortas (MU-NA). Our multiphasic model shows that effective solute diffusivity is increased in MU-NA aortas compared to all others. Our findings reveal changes in intrinsic transport properties that depend on aneurysm severity and are important for understanding the movement of fluids and solutes that may play a role in the diagnosis, progression, or treatment of TAA.

Keywords Hydraulic permeability · Effective diffusivity · Mixture theory · Biphasic · Multiphasic · Elastic fibers

1 Introduction

Thoracic aortic aneurysms (TAAs) pose a critical public health concern with an incidence rate of 5.3 per 100,00 individuals/year and a rupture rate of 1.6 per 100,000 individuals/year (Gouveia e Melo et al. 2022). Current treatment guidelines recommend surgery at specified diameters or dilation rates. However, optimal surgical timelines vary depending on patient-specific factors like genetic mutations, sex, and comorbidities (Isselbacher et al. 2022). Independent of etiology, loss of smooth muscle cells (SMCs) and elastic fiber degeneration are commonly observed in TAAs (Isselbacher 2005).

Elastic fibers, in the medial (middle) section of the aortic wall, are extracellular matrix (ECM) components organized in layers that alternate with SMCs to form lamellar units (Wolinsky and Glagov 1967). These elastic fibers provide reversible elasticity to the artery and are thought to physically isolate the SMCs (Yanagisawa and Wagenseil 2020). Although the bulk of mass transport across the aortic wall is regulated by the endothelial cells (ECs) lining the lumen of the aorta, EC dysfunction and impaired barrier function have been demonstrated in mouse models of TAA (Yang et al. 2023). Circulating blood-borne solutes may have increased transport across the aortic wall due to EC dysfunction and elastic fiber degeneration that plays a role in TAA progression (Michel et al. 2007, 2018). For example, plasminogen protein was present in higher concentrations in the medial

✉ Jessica E. Wagenseil
jessica.wagenseil@wustl.edu

[1] Department of Biomedical Engineering, Washington University, St. Louis, MO, USA

[2] Department of Orthopedic Surgery, Washington University, St. Louis, MO, USA

[3] Department of Mechanical Engineering and Materials Science, Washington University, One Brookings Dr., CB 1185, St. Louis, MO 63130, USA

Published online: 29 October 2024

layer of human TAA compared to control, even though plasminogen mRNA was undetectable, implying transport from the blood (Borges et al. 2010). Plasminogen is converted to plasmin within the aortic wall that can cause SMC apoptosis and ECM degradation exacerbating TAA progression (Boukais et al. 2018a, b).

We have shown experimentally that transmural fluid and 4 kDA FITC-dextran solute flux are altered in the ascending thoracic aorta (Crandall et al. 2022, 2023) and carotid artery (Cocciolone et al. 2018) in chemical and genetic mouse models of elastic fiber fragmentation associated with TAA. Using a $Fbln4^{E57K/E57K}$ mouse model of TAA (Igoucheva et al. 2015), we showed that transmural fluid and solute flux depend on the presence of the genetic mutation associated with fragmented elastic fibers and on aneurysm severity (Crandall et al. 2023). However, our experimental results could not isolate competing factors, such as changes in geometry and solid material properties of the aortic wall amongst these mouse models, to determine how intrinsic transport properties change with aneurysm severity.

Continuum models of biphasic and multiphasic materials have been developed to understand how intrinsic solid and fluid properties of soft tissues, including strain-dependent porosities, hydraulic permeability, and effective solute diffusivities, govern fluid and solute flux (Holmes and Mow 1990; Ateshian et al. 2012; Lai et al. 1991). We previously developed a multiphasic model of the denuded (ECs removed) carotid arterial wall as a continuum mixture of solid, fluid, and solute phases to determine intrinsic transport properties, hydraulic permeability and effective diffusivity, as a function of genetic and chemical disruption of the elastic fibers (Guang et al. 2022). However, the model did not include expansion of the arterial wall due to an applied pressure or case-specific geometry and characterization of the effects of solid wall material properties.

Here, we use FEBio (Maas et al. 2012) to develop biphasic and multiphasic models of the ascending aortic wall with experimentally measured geometries and mass transport data from our prior experimental work using the $Fbln4^{E57K/E57K}$ TAA mouse model (Crandall et al. 2023). The objective of this study is to distinguish competing factors that may influence transmural fluid and solute flux and reveal changes in intrinsic transport properties in TAA that may explain our experimental results. The biphasic model allows us to characterize how the fluid moves relative to the solid phase in the aortic wall of our mouse models with varying genetic mutations and aneurysm severity. The multiphasic model further allows characterization of solute movement across the aortic wall given altered fluid–solid interactions in our different mouse models. We determine how hydraulic permeability and effective solute diffusivity of the ascending aortic wall depend on TAA severity in mouse models of human disease.

2 Methods

2.1 Mouse model

We previously published experimental transmural transport data for the ascending aortic wall in mouse models of TAA with varying severity (Crandall et al. 2023). We used mice with a clinically identified missense mutation ($Fbln4^{E57K/E57K}$) in the *Efemp2* gene which encodes the fibulin-4 protein that is partially responsible for ECM assembly and elastogenesis in the aortic wall (Igoucheva et al. 2015). $Fbln4^{E57K/E57K}$ mice have 50% TAA penetrance and elastic fiber fragmentation. Fibulin-4 interacts with lysyl oxidase (LOX) during elastogenesis to form elastic fibers. To increase aneurysm severity, we bred the $Fbln4^{E57K/E57K}$ mice with *Lox* haploinsufficient mice ($Lox^{+/-}$) (Hornstra et al. 2003), hypothesizing that decreased lysyl oxidase would increase aneurysm penetrance. We observed 100% aneurysm penetrance in the $Fbln4^{E57K/E57K}$;$Lox^{+/-}$ mice. We performed transport experiments on the ascending aorta from four experimental groups: $Fbln4^{+/+}$;$Lox^{+/+}$ (WT), $Fbln4^{E57K/E57K}$;$Lox^{+/+}$ without an aneurysm (MU-NA), $Fbln4^{E57K/E57K}$;$Lox^{+/+}$

Table 1 Cases are defined by the genotype and presence or absence of aneurysmal dilation

Case	Genotype	Aneurysm penetrance (%)	Elastic fiber fragmentation (Y/N)	Length (l) (mm)	Outer radius (R_o) (mm)	Thickness (T) (mm)
WT	$Fbln4^{+/+}$	0	N	1.63 ± 0.29	0.42 ± 0.13	0.11
MU-NA	$Fbln4^{E57K/E57K}$	50	Y	3.27 ± 0.43	0.46 ± 0.08	0.13
MU-A				3.92 ± 0.71	0.76 ± 0.15	0.13
MU-XA	$Fbln4^{E57K/E57K}$; $Lox^{\pm}$	100	Y	4.26 ± 1.03	0.76 ± 0.14	0.13

The genotype, aneurysm penetrance, and elastic fiber fragmentation are listed, as well as the experimentally derived length and unloaded outer radius (mean ± SD) and thickness (Halabi et al. 2017; Crandall et al. 2023)

with aneurysm (MU-A), and $Fbln4^{E57K/E57K};Lox^{+/-}$ with aneurysm (MU-XA) (Table 1).

2.2 Experimental transport measurements

Detailed experimental methods can be found in (Crandall et al. 2023). Briefly, we euthanized 3–4-month-old male and female mice by carbon dioxide inhalation. All animal procedures were approved by Washington University's Institutional Animal Care and Use Committee. The ascending thoracic aorta was dissected, placed in phosphate-buffered saline (PBS) at 4 °C, and tested within 72 h of dissection. The aorta was fixed onto cannulae using 7–0 sutures in a pressure myograph (110P, Danish Myo Technology) and placed in a 7-mL PBS bath at 37 °C. The myograph was pressurized to the mean mouse blood pressure of 13.33 kPa using a static fluid column and stretched to 1.1 × axial stretch (Wagenseil et al. 2005). Fluid flux (J_v) was measured by introducing a bubble into the lead tubing of the myograph to measure the bubble's velocity as fluid permeated through the aortic wall. To study transport of a solute, PBS in the static column was replaced with 1.25 mM 4 kDa fluorescein isothiocyanate (FITC)-dextran dissolved in PBS (Sigma-Aldrich; #46944) and the myograph was again pressurized to 13.33 kPa using the static column. Concentration of the 4 kDa FITC-dextran in the bath over time was measured using a fluorescent plate reader (MolecularDevices, SpectraMax M2e) to determine solute flux (J_s) through the aortic wall. Experimental values of transmural fluid flux (J_v) and solute fluid flux (J_s) are summarized in Table 2 (Crandall et al. 2023).

2.3 Aortic wall geometry

For construction of the computational models, unloaded inner and outer radii are required. In our experiments, we recorded the outer radii and thickness at 13.33 kPa and length at 1.1 × axial stretch (Crandall et al. 2023). Using previously published pressure-diameter curves for $Fbln4^{E57K/E57K}$ ascending thoracic aorta from Dr. Carmen Halabi, the average outer radius at 0 kPa was obtained for WT, MU-NA, and MU-A (Halabi et al. 2017). We assumed that the MU-XA aorta had the same unloaded outer radius as the MU-A aorta, since the loaded outer radii at 13.33 kPa are similar. As axial stretch ratio was not recorded in the pressure-diameter curves (Halabi et al. 2017), we assumed that it was similar to the 1.1 × axial stretch used in Crandall et al. (2023). Unloaded inner radii were determined assuming an incompressible hollow cylinder. The starting geometry for the models was the average length of the ascending aorta between cannulae recorded for the experimental data (Crandall et al. 2023) and the average calculated unloaded radii for each case (Table 1).

Table 2 Average experimental measurements for fluid (J_v) and solute (J_s) flux (mean ± SD) (Crandall et al. 2023)

Case	Fluid Flux, $J_v\left[10^{-4}\frac{mm}{s}\right]$	Solute Flux, J_s $\left[10^{-7}\frac{\mu mol}{mm^2 * s}\right]$
WT	7.57 ± 2.57	0.97 ± 0.76[#]
MU-NA	4.96 ± 1.42	4.85 ± 2.06[&]
MU-A	3.01 ± 0.80[&]	2.26 ± 0.84[#]
MU-XA	2.40 ± 0.62[&]	0.80 ± 0.53[#]

[&]indicates significant difference from WT and [#]indicates significant difference from MU-NA

2.4 Aortic wall solid material properties

The unconstrained Holzapfel-Gasser-Ogden (HGO) constitutive relation (Gasser et al. 2006) available in FEBio (Maas et al. 2012) was chosen to model the nonlinear solid mechanical behavior of the aortic wall. The HGO relation includes a Neo-Hookean isotropic solid with two symmetric families of exponentially behaving embedded fibers. The FEBio implementation of the unconstrained HGO constitutive relation allows for pore volume changes in response to fluid flux. The strain energy function (Ψ) for the solid material is given by:

$$\Psi = \frac{c}{2}(I_1 - 3) - c\ln J + \frac{k_1}{2k_2}\sum_{i=1}^{2}\left[exp\left\{k_2\left[\kappa I_1 + (1-3\kappa)I_{4i} - 1\right]^2\right\} - 1\right] + \frac{K_0}{2}\left(\frac{J^2-1}{2} - \ln J\right) \quad (1)$$

where c is the Neo-Hookean material constant, $I_1 = tr(\boldsymbol{F}^T\boldsymbol{F})$ and $\mathbf{F}$ is the deformation gradient tensor, $J = \det \mathbf{F}$ is the volume ratio, and k_1 and k_2 are fiber material constants. κ characterizes the fiber dispersion ranging from 0 (no dispersion) to 1/3 (isotropic dispersion) (Gasser, Ogden, and Holzapfel 2006). $I_{4i} = \lambda_\theta^2 cos^2\gamma + \lambda_z^2 sin^2\gamma$ describes the stretch along the fiber direction oriented at angle $\pm\gamma$ degrees (i = 1, 2) to the circumferential direction and λ_θ, λ_z are the aortic stretch ratios in the circumferential and axial directions, respectively. The fibers only support positive strain. K_0 is the bulk modulus of the isotropic Neo-Hookean solid and is set to 1000 × greater than c in FEBio to ensure that the solid tissue is intrinsically incompressible (Altundemir et al. 2023).

As we did not have the necessary stretch-stress data for the mouse aortae used in this study to fit HGO material parameters, we used previously published data from Bellini et al. (2016) for the ascending aorta from a different genetic model of TAA ($Fbn1^{mgR/mgR}$) (Pereira et al. 1999) with and without aneurysms and wild-type controls. We used the material parameters and 4-fiber constitutive relation in Bellini et al. (2016) and circumferential and

axial stretch ratios from previous studies in our laboratory (Kailash et al. 2024) to generate pseudo-stretch-stress data. We then used nonlinear optimization in MATLAB to minimize differences between the pseudo-stretch-stress data and the HGO predicted stretch-stress values to obtain approximate material parameters for the HGO constitutive relation for WT, MU-NA, and MU-A aortae.

We created structural models of the ascending aorta for each case using the measured cylindrical geometry (Table 1) and approximate HGO parameters in FEBio (Maas et al. 2012). We assumed that MU-XA aorta would be similar to but "stiffer" than MU-A aorta so that k_1 would be increased by 44%. To simulate our experimental set-up where we tie the aorta onto cannulae, zero-displacement boundary conditions in all directions were imposed at the long ends of the cylinder. We examined the structural model results at a point midway along the aortic length where edge effects were negligible. We adjusted the approximate HGO parameters to match measures of luminal pressure and outer diameter (Halabi et al. 2017) (Fig. 1A). We then calculated the resulting circumferential stretch (λ_θ) and stress (σ_θ) at an element midway across the aortic wall thickness (Fig. 1B) to ensure the pattern of predicted behavior matched that observed for wild-type, aneurysmal, and non-aneurysmal mouse aorta (Bellini et al. 2016). We also calculated the deformed thickness at 13.33 kPa from the structural models to compare to our experimental results (Crandall et al. 2023) (Fig. 1C). We used these final HGO parameters (Table 3) for the biphasic (Sect. 2.5) and multiphasic (Sect. 2.6) models for each case.

2.5 Biphasic model

A biphasic model of the aortic wall was constructed in FEBio (Maas et al. 2012). The experimental set-up was modeled by considering the aorta as a hollow cylinder fully interfaced with a 7-mL external collecting bath (Fig. 2A) and case-specific geometry (Table 1). Zero-displacement boundary conditions in all directions were imposed at the ends of the cylinder. The aortic wall was meshed using eight-node hexahedral elements refined radially closer to the inner and outer radius. The 7 mL collecting bath was also meshed using eight-node hexahedral elements refined

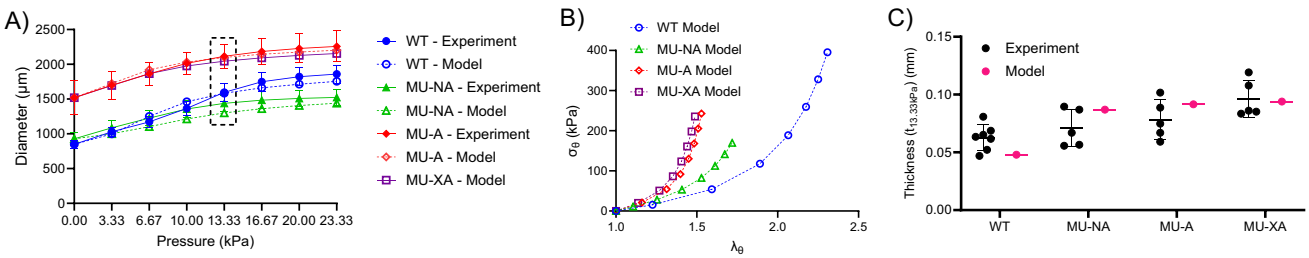

Fig. 1 Solid mechanical behavior of the aortic wall. Using case-specific geometry (Table 1) and unconstrained HGO parameters (Table 3) for each case, we show the **A** experimental (Halabi et al. 2017) and model predicted luminal pressures vs. outer diameter behavior and highlight (dashed box) the 13.33 kPa luminal pressure used for the transport experiments in Crandall et al. (2023). Halabi et al. (2017) did not include MU-XA experimental data, so we assume it is similar to MU-A based on the diameter at 13.33 kPa reported in Crandall et al. (2023). **B** Model-predicted mid-wall, mid-length circumferential stretch (λ_θ) vs. stress (σ_θ) for each applied pressure for each case. **C** Deformed thickness at 13.33 kPa from the experimental data in Crandall et al. (2023) and predicted by the model

Table 3 Unconstrained Holzapfel–Gasser–Ogden (HGO) material parameters for each case

Case	c (kPa)	k_1 (kPa)	k_2	γ(°)	κ	K_0(kPa)
WT	15	3	0.1	23	0.1	15,000
MU-NA	23	20	1	24	0.26	23,000
MU-A	24	9	1.7	34	0.01	24,000
MU-XA	24	13	1.7	34	0.01	24,000

Values were calculated using the material parameters and 4-fiber constitutive relation in Bellini et al. (2016) along with circumferential and axial stretch ratios from Kailash et al. (2024) to generate pseudo-stretch-stress data for WT, MU-NA, and MU-A cases. We used nonlinear optimization to fit approximate HGO material parameters to the pseudo-stretch-stress data and adjusted them to match the experimental pressure-diameter data, expected stretch-stress behavior, and deformed thicknesses (Fig. 1). We assumed that the MU-XA aorta would be similar to, but "stiffer" than MU-A aorta so that k_1 would be increased. The bulk modulus, *Ko*, was chosen as $1000 \times c$ to ensure incompressibility

A)

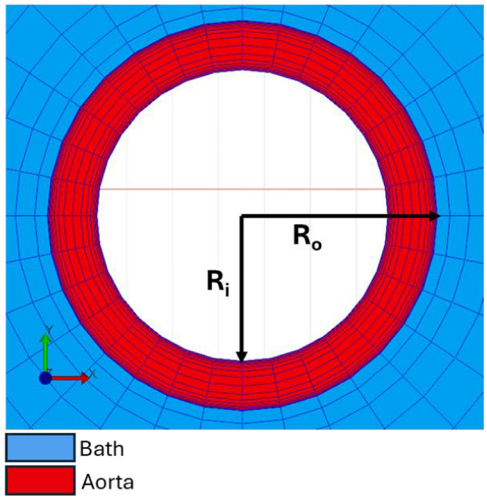

B)

Biphasic and Multiphasic Baseline Model Parameters		
	Aortic Wall	Bath
Solid Volume Fraction (φ_0)	0.6	0
Osmotic Coefficient (ϕ)	1	1
Material Model	Unconstrained HGO	Neo-Hookean
Material Parameters	Table 3	E = 0.01 kPa ν = 0.49
Permeability Model	Constant-Isotropic	
Hydraulic Permeability (k_o) $\left[\frac{mm^4}{mN \cdot s}\right]$	Optimized in biphasic	1
Diffusion Model	Constant-Isotropic	
d_0 $\left[\frac{mm^2}{s}\right]$	$2.34x10^{-4}$	2.34
d_{eff} $\left[\frac{mm^2}{s}\right]$	Optimized in multiphasic	2.34

Fig. 2 Model geometry and variables. **A** The aortic wall is modeled as an axisymmetric cylinder (red) with a case specific outer (R_o) and inner (R_i) radius shown in Table 1. The bath (blue) is modeled as an incompressible fluid with a 7-mL volume. **B** Baseline biphasic and multiphasic parameters for the aortic wall and the bath

closer to the inner radius. The mesh densities were chosen to satisfy mesh convergence and independence.

Baseline material properties for the biphasic and multiphasic representations of the aortic wall and collecting bath are given in Fig. 2B. An unconstrained HGO solid material model was used for the aortic wall, and parameters were determined as described in Sect. 2.4. The solid volume fraction of the aortic wall was set to $\varphi_0 = 0.6$, as determined from previous experiments (Chooi et al. 2016) and modeling (Guang et al. 2022). The collecting bath was modeled as an incompressible, isotropic Neo-Hookean solid with $E = 0.01$ kPa, $\nu = 0.49$, $\varphi_0 = 0$ (no solid volume fraction) to represent the fluid phase. The aortic wall and collecting bath were given constant isotropic permeability $\boldsymbol{k}$ where $\boldsymbol{k} = k_o\boldsymbol{I}$ and k_o is the isotropic hydraulic permeability and $\boldsymbol{I}$ is the identity tensor. k_o for the aortic wall was optimized from experimental data (Sect. 2.7) and k_o for the collecting bath was set to $1\,\frac{mm^4}{mN \cdot s}$.

In the system, the total mixture stress ($\boldsymbol{\sigma}$) is related to both the hydraulic fluid pressure (p) and the solid matrix stress ($\boldsymbol{\sigma}^e$),

$$\boldsymbol{\sigma} = -p\boldsymbol{I} + \boldsymbol{\sigma}^e, \tag{2}$$

where the solid matrix is determined by the strain energy function (Eq. 1) and the deformation. The volumetric fluid flux ($\boldsymbol{w}$) of the fluid relative to the solid in the biphasic model is,

$$\boldsymbol{w} = -\boldsymbol{k} \cdot (\nabla p), \tag{3}$$

where ∇ is the gradient. To match the experimental conditions (Crandall et al. 2023), we prescribed a fluid pressure boundary condition of $p = 13.33$ kPa at the inner nodes of the aortic wall and $p = 0$ kPa via a zero fluid pressure boundary condition at the outermost nodes of the collecting bath. For a biphasic surface with a non-zero fluid pressure, corresponding mixture traction must be applied. The normal component of the mixture traction (t_n) was prescribed as $t_n = -13.33$ kPa to the inner elements of the aortic wall (Maas et al. 2024).

2.6 Multiphasic model

A multiphasic model was created using similar procedures, displacement boundary conditions, and material properties to those described above (Fig. 2) with the addition of a concentration gradient due to the 1.25 mM 4 kDa FITC-dextran that was added to the lumen of the aorta in the experiments (Crandall

et al. 2023). The solute has access to all pore spaces of the solid matrix. In the multiphasic model, the volumetric flux ($\boldsymbol{w}$) of the solvent relative to the solid is,

$$\boldsymbol{w} = -\tilde{\boldsymbol{k}} \cdot \left(\nabla \tilde{p} + R\theta \frac{\boldsymbol{d}}{d_0} \cdot \nabla \mathrm{C} \right), \tag{4}$$

with the effective fluid pressure ($\tilde{p}$) defined by,

$$\tilde{p} = p - R\theta\phi C, \tag{5}$$

and

$$\tilde{\boldsymbol{k}} = \left[\boldsymbol{k}^{-1} + \frac{R\theta}{\varphi^w} \frac{C}{d_0} \left(\boldsymbol{I} - \frac{\boldsymbol{d}}{d_0} \right) \right]^{-1}, \tag{6}$$

where R is the gas constant, θ is the absolute temperature, $\boldsymbol{d} = d_{eff}\boldsymbol{I}$ assuming constant isotropic diffusivity, d_0 is the solute free diffusivity, C is the concentration of the solute, ϕ is the osmotic coefficient and is assumed to be unity. φ^w is the mobile fluid fraction where $\varphi^w = 1 - \varphi^s$, and φ^s is the solid matrix volume fraction in the current state. The solute free diffusivity was calculated using the Stokes–Einstein equation,

$$d_0 = \frac{k_B \theta}{6\pi r_s \eta}, \tag{7}$$

where k_B is Boltzmann's constant, r_s is the solute's hydrodynamic radius, and η is the dynamic viscosity of the solvent (Miller 1924). We previously showed that the hydrodynamic radius of 4 kDA FITC-dextran is close to the radius of 1.4 nm measured by the manufacturer (Guang et al. 2022). The viscosity of PBS at 310 K was assumed to match that of water ($(6.92 \times 10^{-4} \frac{kg}{m*s}$); hence $d_0 = 2.34 \times 10^{-4} \frac{mm^2}{s}$ (Fig. 2B). The effective solute diffusivity (d_{eff}) was optimized from the experimental data (Sect. 2.7).

The molar flux ($\mathbf{j}$) of the solute relative to the solid in the multiphasic model is given by,

$$\boldsymbol{j} = \boldsymbol{d} \cdot \left(-\varphi^w \nabla \mathrm{C} + \frac{C}{d_0} \boldsymbol{w} \right) \tag{8}$$

To match the experimental conditions for the multiphasic model we prescribed effective fluid pressure $\widetilde{p} = 10.11$ kPa at the inner nodes of the aortic wall and hydraulic fluid pressure $p = 0$ kPa via a zero fluid pressure boundary condition at the outermost nodes of the collecting bath. We prescribed $t_n = -13.33$ kPa to the inner elements of the aortic wall, as in the biphasic model. In the collecting bath, we set d_0 to be 10,000 × higher than d_0 in the aortic wall to simulate well-mixed conditions and set $d_{eff} = d_0$ because the collecting bath has no resistance to solute flux.

2.7 Optimizing transport material properties

The constrained Levenberg–Marquardt optimization algorithm in FEBio was utilized to obtain the hydraulic permeability (k_0) by optimizing biphasic predictions of fluid flux at the outer wall ($\boldsymbol{w}$) to experimental measures of fluid flux (J_v) for each aorta. After determining k_0 for each aorta using the biphasic model, the constrained Levenberg–Marquardt optimization algorithm in FEBio was used to determine d_{eff} for each aorta by optimizing multiphasic predictions of transient concentration to experimental measures of transient concentration. We evaluated the ability of our multiphasic model to match experimental solute findings by comparing our multiphasic solute flux ($\boldsymbol{j}$) to our experimental solute flux (J_s). The objective of this study was to determine if k_0 and d_{eff}, which are intrinsic transport properties, are altered in mouse models of TAA.

2.8 Statistical analysis

One-way ANOVA and Tukey's post-hoc test were used to test for differences in k_0 and d_{eff} between the four cases (WT, MU-NA, MU-A, MU-XA) at a significance level of 0.05 (Prism, GraphPad).

3 Results

3.1 Experimental results

Experimental results for fluid and solute flux have previously been published and are summarized in Table 2 (Crandall et al. 2023).

3.2 Biphasic model parameter sweep

To understand how different factors contribute to the transmural fluid flux, we varied the undeformed thickness (0.11 – 0.13 mm), φ_0 (0.3–0.9), unconstrained HGO parameters, and k_0 ($1 \times 10^{-7} - 1 \times 10^{-5} \frac{mm^4}{mN \cdot s}$) and calculated the transmural fluid flux for the biphasic model. Unless otherwise noted, we used WT geometry and HGO parameters for the biphasic model parameter sweep. The parameter ranges represent differences between cases (Tables 1 and 3) and expected experimental values based on previous work (Guang et al. 2022; Chooi et al. 2016). As thickness increases from the minimum of 0.11 mm to the maximum of 0.13 mm (Table 1), fluid flux decreases by 29% (Fig. 3A), indicating that thickening of the aortic wall in MU mice partially contributes to the reduced fluid flux observed experimentally (Table 2). Across the ranges tested, φ_0 has no effect on fluid flux (Fig. 3B). The case-specific HGO parameters (Table 3) decrease the fluid flux by 28%

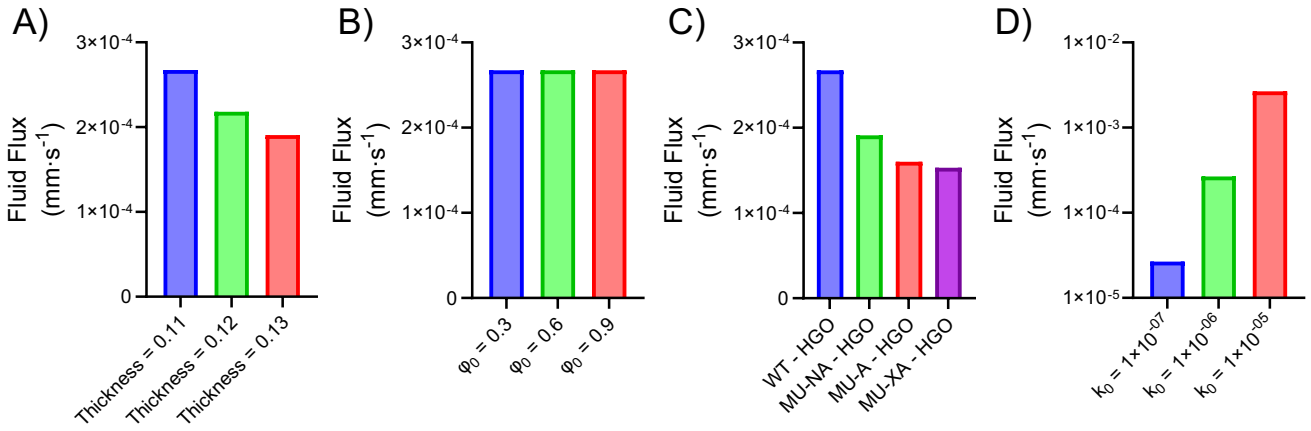

Fig. 3 Parametric sweep for the biphasic model showing effects of varied **A** undeformed wall thickness (mm), **B** solid volume fraction (φ_0), **C** HGO parameters (Table 3), and **D** reference hydraulic permeability (k_0) $(\frac{mm^4}{mN \bullet s})$ on fluid flux. Panel D is plotted on a log scale. Unless otherwise noted, the model included WT geometry and HGO parameters (Tables 1 and 3) and the following mass transport parameters: $\varphi_0 = 0.6$ and $k_0 = 1 * 10^{-6} \frac{mm^4}{mN \bullet s}$

in MU-NA, 40% in MU-A, and 43% in MU-XA compared to WT (Fig. 3C), demonstrating a geometry independent effect of the solid material parameters on fluid flux. k_0 has the largest effect on fluid flux, increasing it ninefold over the range tested (Fig. 3D). These observations indicate that k_0 is a critical parameter to determine for fluid flux predictions across the aortic wall.

3.3 Determination of hydraulic permeability

We solved for k_0 by optimizing our biphasic $\boldsymbol{w}$ against our experimental values of J_v using case-specific geometry and unconstrained HGO material properties (Tables 1 and 3). We found a 49% decrease in k_0 for MU-XA compared to MU-NA aortas (Fig. 4A). The experimentally derived fluid flux and biphasic model-simulated fluid fluxes are shown in Fig. 4B. The average absolute percent difference between the experimental and model-simulated fluid fluxes was 0.08% for all aortas.

3.4 Multiphasic model parameter sweep

We next explored how undeformed thickness, φ_0, unconstrained HGO parameters, k_0, and d_{eff} affect transmural solute flux. Unless otherwise noted, we used WT geometry and HGO parameters for the multiphasic model parameter sweep. Increasing undeformed thickness from the minimum of 0.11 mm to the maximum of 0.13 mm (Table 1) decreases solute flux by 29% (Fig. 5A). This is opposite to the changes observed experimentally for increased solute flux in the thickened MU aorta compared to WT (Table 2), highlighting the importance of controlling for geometric effects. Increasing φ_0 from 0.3 to 0.9 reduces solute flux by 71% (Fig. 5B). The case-specific HGO parameters (Table 3)

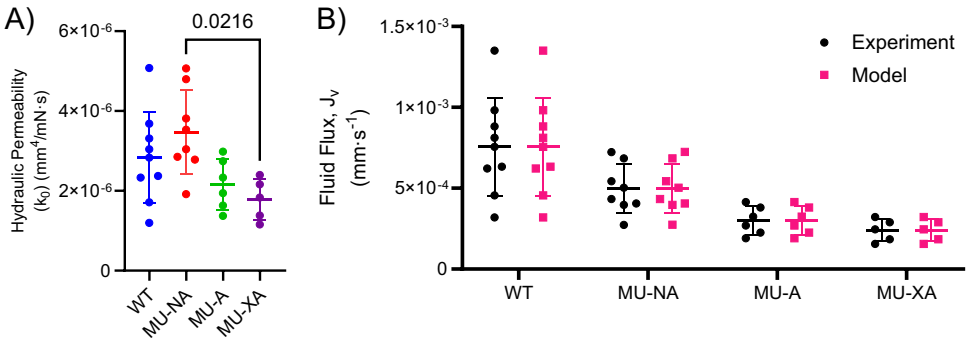

Fig. 4 Results of the biphasic model. **A** Hydraulic permeability values (k_0) were determined from fitting the model to the fluid flux (J_v) data for each experimental case. *P*-values shown for $p < 0.05$. Significance was determined using a one-way ANOVA followed by Tukey's post-hoc test. The hydraulic permeability in the MU-XA group was significantly lower than in the MU-NA group. **B** Fluid flux comparison between model-predicted and experimental values. N = 5–9/group. Model parameters are given in Fig. 2B

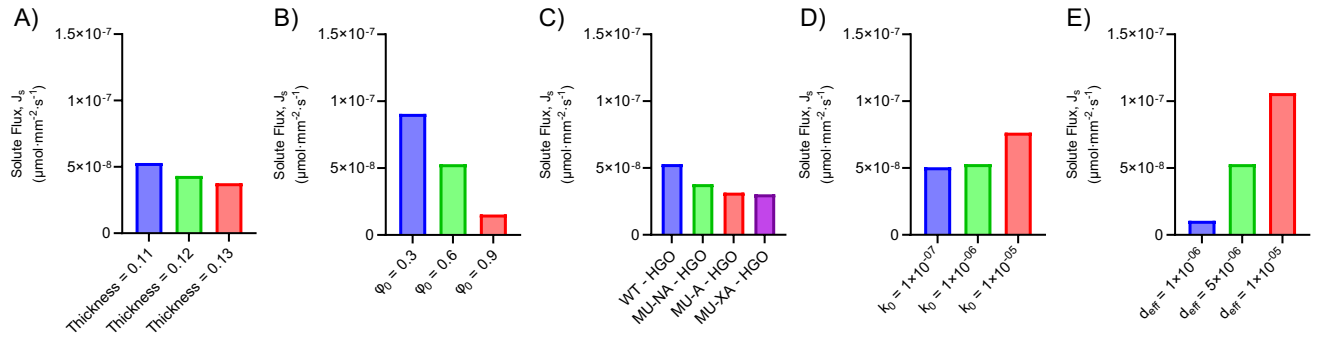

Fig. 5 Parametric sweep for the multiphasic model showing effects of varied **A** undeformed wall thickness (mm), **B** solid volume fraction (φ_0), **C** HGO parameters (Table 3), **D** reference hydraulic permeability $(k_0)(\frac{mm^4}{mN \bullet s})$, and E) effective diffusivity (d_{eff}) $(\frac{mm^2}{s})$ on solute flux. Unless otherwise noted, the model included WT geometry and HGO parameters (Tables 1 and 3) and the following mass transport parameters: $\varphi_0 = 0.6, k_0 = 1 * 10^{-6} \frac{mm^4}{mN \bullet s}$, and $d_{\text{eff}} = 5 * 10^{-6} \frac{mm^2}{s}$.

decrease the solute flux 28% in MU-NA, 40% in MU-A, and 43% in MU-XA compared to WT (Fig. 5C), which is again opposite to the experimentally observed changes in the MU cases compared to WT (Table 2). There is a 51% increase in solute flux as k_0 increases from $1 \times 10^{-7} \frac{mm^4}{mN \bullet s}$ to $1 \times 10^{-5} \frac{mm^4}{mN \bullet s}$ (Fig. 5D). As d_{eff} increases from $1 \times 10^{-6} \frac{mm^2}{s}$ to $1 \times 10^{-5} \frac{mm^2}{s}$, there is a ninefold increase in solute flux. These results show weak dependence of solute flux on undeformed thickness and HGO material parameters, moderate dependence on φ_0 and k_0, and strong dependence on d_{eff}. Thickness values were determined experimentally. Unconstrained HGO material parameters were estimated from previous data (Sect. 2.4). k_0 was determined from optimization of the experimental fluid flux to the biphasic model fluid flux. d_{eff} was determined from optimization of the experimental transient concentration to the multiphasic model transient concentration. While solute flux is dependent on φ_0, in the absence of physiologic data we set $\varphi_0 = 0.6$, as has been found experimentally (Chooi et al. 2016) and we have done previously (Guang et al. 2022).

3.5 Determination of effective solute diffusivity

We used the optimized k_0 for each aorta and determined d_{eff} from nonlinear optimization using the experimental transient concentration data (Fig. 6A). This yielded an aorta-specific k_0 and d_{eff} across all four cases. d_{eff} is significantly increased in MU-NA aorta compared to all other groups, but neither aneurysmal group (MU-A or MU-XA) is different from WT (Fig. 6B). Given k_0 and d_{eff}, the multiphasic model was used to determine a simulated solute flux (Fig. 6C). The average absolute percent difference between the experimental and model-simulated solute flux was 47% for all aortas, with no trend toward over-or under-predicting in each case (average percent difference is -3%). It should be noted that there were variations in the geometry (Crandall et al. 2023) and likely the material behavior for each aortic wall that were not accounted for in our models which used

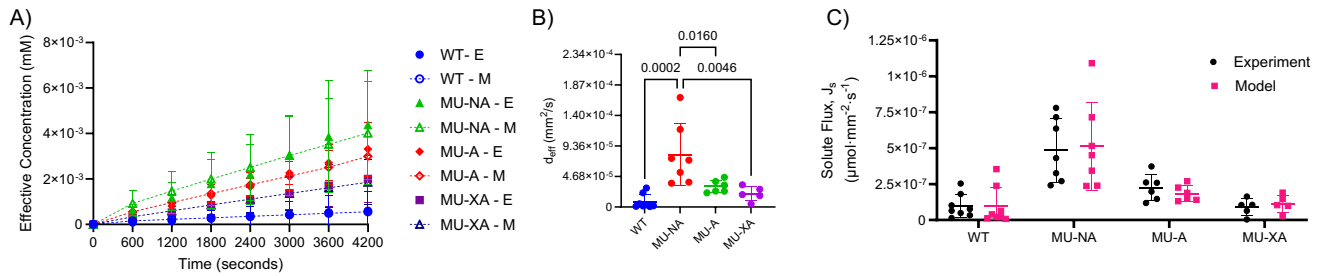

Fig. 6 Results of the multiphasic model. **A** Experimental (E) and model (M) time vs. concentration plots. **B** Optimized d_{eff} values determined from nonlinear optimization to the time vs. concentration data for each aorta. *P*-values shown for $p < 0.05$. Significance was determined by one-way ANOVA followed by Tukey's post-hoc test. d_{eff} for MU-NA aorta is significantly greater than all other groups. **C** Solute flux (J_s) comparison between model predictions and experimental values. N = 5–8/group. Model parameters are given in Fig. 2B

case-specific average geometry and HGO material parameters (Tables 1 and 3). Differences between the average and individual geometries and material parameters could account for some of the differences between the model predictions and experimental results for the solute flux. FEBio models and results for each case with the average fitted k_o and d_{eff} are available at https://doi.org/https://doi.org/10.6084/m9.figshare.27135579.

4 Discussion

Biphasic and multiphasic models were developed to investigate how genetic mutations associated with fragmented elastic fibers affect the relative movement of fluid and 4 kDa FITC-dextran solute across the aortic wall in mouse models of TAA with varying severity. Although changes in vascular geometry and solid material properties of the wall for the various cases partially contribute to changes in transmural fluid and solute flux, our findings reveal changes in intrinsic transport properties, k_0 and d_{eff}, that depend on the presence or absence of aneurysmal dilation in each case. In particular, k_0 is lower in the most extreme aneurysm aortas (MU-XA), with elastic fiber fragmentation and 100% aneurysm phenotype, than in MU-NA aortas, with fragmented elastic fibers and no aneurysmal dilation. Interestingly, WT and MU-NA aortas have similar k_0 indicating that changes in wall thickness (Fig. 3A) and/or solid material properties (Fig. 3C) can explain the differences in fluid flux (Fig. 4B). MU-NA aortas have significantly higher d_{eff} than WT controls and both aneurysmal groups indicating that changes in wall thickness (Fig. 5A) and/or solid material properties (Fig. 5C) cannot explain the differences in solute flux (Fig. 6C). The use of the unconstrained HGO material for the aorta allows us to model the nonlinear pressure-diameter and stress-stretch response of the aorta (Fig. 1A, B) over a range of pressures creating a realistic loaded geometry for the fluid- and solute flux simulations. The results indicate aortic wall remodeling associated with fragmented elastic fibers and TAA dilation that affects transmural fluid and 4 kDa FITC-dextran solute movement.

4.1 ECM remodeling and intrinsic transport properties

As shown in our previous work (Guang et al. 2022), fluid flux is affected minimally by φ_0 and solid material properties, but depends highly on k_0. Although only significant for MU-XA aortas compared to MU-NA, there is a trend toward decreased k_0 in MU-A aortas, as well. Decreased k_0 suggests that ECM remodeling in response to genetic mutations that affect elastic fiber assembly and resulting remodeling seen with aneurysmal dilation may hinder fluid movement through the aortic wall. Previous research shows massive proteoglycan deposition, in particular aggrecan and versican, in the aneurysmal aortic wall of mice and humans (Cikach et al. 2018). At high concentrations, proteoglycans create a large osmotic swelling pressure and draw water into the tissue, which then increases resistance to fluid flow and redistribution of water (Kiani et al. 2002). There is evidence of proteoglycan deposition in the MU-XA aorta (Crandall et al. 2023). It is possible that increased proteoglycans in the TAA wall sequester intra-wall fluid, decreasing the mobile fluid fraction, and reducing k_0. In that case, k_0 may be a biomarker of wall remodeling associated with TAA.

Our calculated d_{eff} values, a measure of the mobility of a solute through a porous medium, are the same order of magnitude as our previous work (Guang et al. 2022). Our d_{eff} values are also the same order of magnitude as those of the bovine internal carotid artery for similar molecular weight solutes (Hwang and Edelman 2002). d_{eff} of MU-NA aortic wall is significantly greater than WT, whereas neither aneurysmal group (MU-A and MU-XA) is different from WT. Although not significant, MU-A and MU-XA aortae have trends toward increasing d_{eff} compared to WT. It is tempting to speculate that ECM wall remodeling leads first to changes that facilitate solute movement when there are genetic mutations associated with TAA but no dilation (MU-NA), then as TAA develops (MU-NA and MU-XA) additional wall remodeling leads to changes that hinder solute movement. As many ECM proteins and fragments of ECM proteins can bind and sequester molecules, it is possible that dynamic changes occur in TAA formation that alter d_{eff}. This should be investigated in a temporal fashion throughout TAA formation in a single mouse model, rather than multiple mouse models with varying TAA phenotypes, as we did in this study. Additionally, different solutes may be uniquely affected by dynamic ECM remodeling and the observed changes in proteoglycan fraction, so we can expect that the charge, as well as molecular weight and other characteristics will affect solute transport.

Prior efforts by Edelman and colleagues characterized transport in the ex vivo aortic wall. They found that solute characteristics, like hydrophobicity or hydrophilicity, affect tissue concentrations and transmural transport (Lovich et al. 1998; Hwang and Edelman 2002; Levin et al. 2004). Similar to our multiphasic sweep results, they found that convective mechanisms (i.e. k_0) are significant determinants of transmural heparin (solute) transport (Lovich et al. 1998). These studies illustrate that the driving factors (i.e. blood pressure and concentration), the geometry and structural composition of the aortic wall, and the solute properties affect transmural transport. Our study builds on prior work by further linking fluid and solute transport to geometry and structural composition of the aortic wall, and further identifying intrinsic

transport parameters that vary according to disease genotype and TAA phenotype.

Histological examination shows a variety of structural changes to the aortic wall in TAA (Yousef et al. 2021; Bellini et al. 2017). In addition to fragmented elastic fibers (Isselbacher 2005) and proteoglycan deposition (Cikach et al. 2018), studies show increased amounts of interstitial collagens and a loss of vascular SMCs; however, specific changes vary according to etiology of the disease. ECM remodeling can lead to changes in mechanical behavior of the aortic wall, exposure of previously hidden integrin-binding sites, chronic SMC activation, leakage and deposition of plasma derived cytokines, and infiltration of immune cells from the lumen and adventitia (Lin and Davis 2023).

Deposition of plasma-derived cytokines and infiltration of immune cells from the lumen may be affected by changes in transmural transport (Michel et al. 2018, 2007). Elevated circulating levels of plasminogen (Boukais et al. 2018), prothrombin (Touat et al. 2008), and complement (Piao et al. 2024) which are known to affect SMC phenotype and downstream signaling have been shown in the wall of human and mouse TAA, suggesting facilitated solute transport. Immune cell infiltration also increases in human (Li et al. 2020) and mouse (Sun et al. 2023) TAA, suggesting facilitated transport of large particles (such as cells) and/or increased chemo-mechanical signaling that attracts immune cells.

Recent efforts have focused on understanding and correlating mechanical changes with wall remodeling over the course of TAA progression (Weiss et al. 2023). However, few studies have characterized transport changes associated with TAA wall remodeling that could be harnessed to optimize delivery of imaging agents (Rastogi et al. 2022) or drugs (Shirasu et al. 2016) to the affected site.

4.2 Hypothesized mechanism and future work

With our results, we propose a mechanism (Fig. 7) that will require significant future work to investigate. We hypothesize that elastic fiber fragmentation associated with the genetic mutations in MU aorta leads to increased d_{eff} as the physical barrier between the lumen and multiple layers of the media are disrupted. Increased d_{eff} allows circulating cytokines to enter the aortic media and interact with SMCs (Michel et al. 2007, 2018). The cytokines stimulate ECM remodeling, including additional elastic fiber degradation and deposition of proteoglycans (Borges et al. 2010, 2009; Boukais et al. 2018a, b). The proteoglycans resist fluid flow (Comper and Williams 1987; Gard et al. 1993), decrease k_0 in the MU-A and MU-XA aortas, and bring d_{eff} back to WT values. Medial calcification that is sometimes observed in TAA (Fletcher et al. 2022) could also serve to lower k_0 and d_{eff}. These alterations to mass transport and associated ECM remodeling may help drive TAA progression. Investigations into specific cytokine levels within the aortic wall, relationships between exposure of SMCs to circulating cytokines and ECM remodeling, the role of proteoglycans in sequestration of intra-wall fluid, and how fluid and solute flux change over TAA progression are needed to support or refute our hypothesis.

Future work that can address our hypothesis includes experimental and computational methods. Cytokine screens can identify changes in circulating blood and the aortic wall throughout TAA progression (Meccanici et al. 2023). In vitro studies can investigate the effects of these cytokines on SMCs and ECM remodeling (Boukais et al. 2018a, b). Proteoglycan deposition can be measured through gene expression studies (Cikach et al. 2018) and Raman microspectroscopy (Sugiyama et al. 2021). Raman

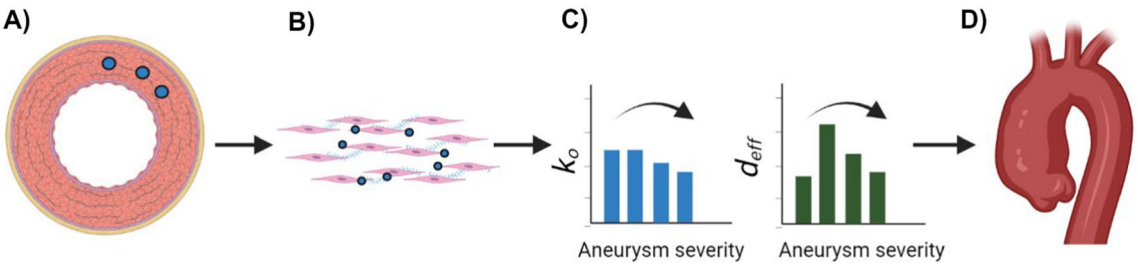

Fig. 7 Hypothesized mechanism. **A** Genetic mutations cause elastic fiber defects increasing d_{eff} and diffusion of circulating cytokines into the aortic wall. **B** These circulating cytokines interact with SMCs and stimulate ECM remodeling, such as proteoglycan deposition, which **C** decreases k_0 and brings d_{eff} back to WT levels. These alterations to mass transport and associated ECM remodeling may drive TAA progression. Created with BioRender.com

microspectroscopy can also be used to measure mobile water fraction (Unal and Akkus 2018). A microstructurally based computational model with SMCs, elastic fibers, collagen fibers, and proteoglycans in the aortic wall (Roccabianca et al. 2014) can investigate how changes in individual components affect fluid and cytokine solute transport.

4.3 Limitations

Our models and experimental data are limited by the absence of an EC layer. ECs regulate transport across the aortic wall, which may be dysregulated in aneurysms (Yang et al. 2023) and was not studied here. We assumed a homogeneous aortic wall (Giannakoulas et al. 2005) although layer specific transport properties for the SMCs and elastic laminae (Tada and Tarbell 2004; Huang and Tarbell 1997) or media and adventitia (Chooi et al. 2016; Hwang and Edelman 2002) have been reported. In the absence of measurements for our mouse models, we assumed constant-isotropic permeability and isotropic diffusivity. Hwang and Edelman illustrated differences in planar and transmural transport of the bovine arterial wall (Hwang and Edelman 2002), so future studies should also investigate varying directional permeability and diffusivity. Altundemir et al. (2023) used a radial strain dependent permeability for human carotid artery that could be investigated for the mouse aorta in future work. Another limitation of our model is the absence of a known φ_0 for each case. Our multiphasic sweep showed that solute flux depends on φ_0, and suggests that future work should attempt to measure φ_0 rather than rely upon a constant value. It is challenging to measure φ_0 by conventional means, like weighing loss of water under compression (Chooi et al. 2016) or fluid displacement by the tissue (Gueldner et al. 2024) as done with porcine aorta.

In terms of the starting geometry, our models could be further improved by considering axial stretch and residual stress. Our starting model length was at the 1.1 × axial stretch reported in Crandall et al. (2023) for all cases. However, it is known that in vivo stretch varies with TAA phenotype in mice (Bellini et al. 2016) and the stretch may affect stress and transport in a nonlinear material. We additionally did not have pressure-diameter behavior for the MU-XA aorta and had to assume material parameters. We considered circumferential expansion and radial compression by incorporating the unloaded radius and thickness and applying a luminal pressure, but we did not consider residual stresses by incorporating opening angles (Chuong and Fung 1986). Residual stresses may be altered by proteoglycan distribution across the aortic wall (Azeloglu et al. 2008) and can affect fluid flux (Altundemir et al. 2023).

5 Conclusions

This study presents a novel approach for characterizing transmural transport differences in the healthy and aneurysmal aortic wall. The use of biphasic and multiphasic models allows us to determine intrinsic transport properties, k_0 and d_{eff}, across a spectrum of aneurysm phenotypes in the mouse. The study advances our understanding of how wall remodeling associated with TAA leads to alterations in transport properties. These intrinsic transport properties are necessary for extending the modeling approach to more realistic geometries (i.e., including ascending aortic curvature), driving forces (i.e., pulsatile flow and pressure), and other organisms (i.e., humans).

Acknowledgements We would like to thank Dr. Carmen Halabi for providing the pressure-diameter curves for the $Fbln4^{E57K/E57K}$ mice. We would like to thank Dr. Victor Barocas and his group for valuable discussions.

Author contributions K.K. contributed to the conception and design of the work, created all computational models, analyzed the data, wrote the main manuscript text, and prepared the figures. S.A. reviewed and modified the computational theory and models. A.D. contributed to the computational theory and interpretation of data. C.C. collected all experimental data and created preliminary computational models. L.C. determined solid material parameters for the aortic wall. L.S. contributed to the conception, design, and implementation of the work. J.W. contributed to the conception, design, implementation, and supervision of the work. All authors critically revised the work, approved the version to be published, and agree to be accountable for all aspects of the work.

Funding This study was supported by National Institutes of Health, R01AR07767804, R01HL133662.

Data availability Data are provided within the manuscript. In addition, multiphasic models for each case are available at https://doi.org/https://doi.org/10.6084/m9.figshare.27135579.

Declarations

Competing interests The authors declare no competing interests.

References

Altundemir S, Lashkarinia SS, Pekkan K, Uguz AK (2023) Interstitial flow, pressure and residual stress in the aging carotid artery model in FEBio. Biomech Model Mechanobiol. https://doi.org/10.1007/s10237-023-01766-7

Ateshian GA, Maas S, Weiss JA (2012) Solute transport across a contact interface in deformable porous media. J Biomech 45:1023–1027. https://doi.org/10.1016/j.jbiomech.2012.01.003

Azeloglu EU, Albro MB, Thimmappa VA, Ateshian GA, Costa KD (2008) Heterogeneous transmural proteoglycan distribution provides a mechanism for regulating residual stresses in the aorta. Am J Physiol Heart Circ Physiol 294:H1197–H1205. https://doi.org/10.1152/ajpheart.01027.2007

Bellini, C., M. R. Bersi, A. W. Caulk, J. Ferruzzi, D. M. Milewicz, F. Ramirez, D. B. Rifkin, G. Tellides, H. Yanagisawa, and J. D. Humphrey (2017) Comparison of 10 murine models reveals a distinct biomechanical phenotype in thoracic aortic aneurysms. J R Soc Interface 14. https://doi.org/10.1098/rsif.2016.1036

Bellini C, Korneva A, Zilberberg L, Ramirez F, Rifkin DB, Humphrey JD (2016) Differential ascending and descending aortic mechanics parallel aneurysmal propensity in a mouse model of Marfan syndrome. J Biomech. https://doi.org/10.1016/j.jbiomech.2015.11.059

Borges LF, Gomez D, Quintana M, Touat Z, Jondeau G, Leclercq A, Meilhac O, Jandrot-Perrus M, Gutierrez PS, Freymuller E, Vranckx R, Michel JB (2010) Fibrinolytic activity is associated with presence of cystic medial degeneration in aneurysms of the ascending aorta. Histopathology 57:917–932. https://doi.org/10.1111/j.1365-2559.2010.03719.x

Borges LF, Touat Z, Leclercq A, Zen AA, Jondeau G, Franc B, Philippe M, Meilhac O, Gutierrez PS, Michel JB (2009) Tissue diffusion and retention of metalloproteinases in ascending aortic aneurysms and dissections. Hum Pathol 40:306–313. https://doi.org/10.1016/j.humpath.2008.08.002

Boukais K, Borges LF, Venisse L, Touat Z, Francois D, Arocas V, Jondeau G, Declerck P, Bouton MC, Michel JB (2018a) Clearance of plasmin-PN-1 complexes by vascular smooth muscle cells in human aneurysm of the ascending aorta. Cardiovasc Pathol 32:15–25. https://doi.org/10.1016/j.carpath.2017.10.002

Boukais, Kamel, Luciano F. Borges, Laurence Venisse, Ziad Touat, Déborah François, Véronique Arocas, Guillaume Jondeau, Paul Declerck, Marie-Christine Bouton, and Jean-Baptiste Michel (2018) Clearance of plasmin–PN-1 complexes by vascular smooth muscle cells in human aneurysm of the ascending aorta. Cardiovasc Pathol 32 15–25. https://doi.org/10.1016/j.carpath.2017.10.002

Chooi, K. Y., A. Comerford, S. J. Sherwin, and P. D. Weinberg (2016) Intimal and medial contributions to the hydraulic resistance of the arterial wall at different pressures: a combined computational and experimental study. J R Soc Interface 13. https://doi.org/10.1098/rsif.2016.0234

Chuong CJ, Fung YC (1986) On residual stresses in arteries. J Biomech Eng 108:189–192

Cikach, F. S., C. D. Koch, T. J. Mead, J. Galatioto, B. B. Willard, K. B. Emerton, M. J. Eagleton, E. H. Blackstone, F. Ramirez, E. E. Roselli, and S. S. Apte (2018) Massive aggrecan and versican accumulation in thoracic aortic aneurysm and dissection. JCI Insight 3. https://doi.org/10.1172/jci.insight.97167

Cocciolone AJ, Johnson E, Shao JY, Wagenseil JE (2018) Elastic fiber fragmentation increases transmural hydraulic conductance and solute transport in mouse arteries. J Biomech Eng. https://doi.org/10.1115/1.4042173

Comper WD, Williams RP (1987) Hydrodynamics of concentrated proteoglycan solutions. J Biol Chem 262:13464–13471

Crandall CL, Kim SY, Rother J, Lee VS, Mecham RP, Wagenseil JE (2022) Increases in hydraulic conductance and solute permeability in a mouse model of ascending thoracic aortic aneurysm. J Biomech 145:111360. https://doi.org/10.1016/j.jbiomech.2022.111360

Crandall CL, Wu Y, Kailash KA, Bersi MR, Halabi CM, Wagenseil JE (2023) Changes in transmural mass transport correlate with ascending thoracic aortic aneurysm diameter in a fibulin-4 E57K knockin mouse model. Am J Physiol Heart Circ Physiol 325:H113–H124. https://doi.org/10.1152/ajpheart.00036.2023

Fletcher AJ, Nash J, Syed MBJ, Macaskill MG, Tavares AAS, Walker N, Salcudean H, Leipsic JA, Lim KHH, Madine J, Wallace W, Field M, Newby DE, Bouchareb R, Seidman MA, Akhtar R, Sellers SL (2022) Microcalcification and thoracic aortopathy: a window into disease severity. Arterioscler Thromb Vasc Biol 42:1048–1059. https://doi.org/10.1161/ATVBAHA.122.317111

Gard TL, Van Buskirk EM, Acott TS (1993) Ionic modulation of flow resistance in an immobilized proteoglycan model of the trabecular meshwork. J Glaucoma 2:183–192

Gasser TC, Ogden RW, Holzapfel GA (2006) Hyperelastic modelling of arterial layers with distributed collagen fibre orientations. J R Soc Interface 3:15–35. https://doi.org/10.1098/rsif.2005.0073

Giannakoulas G, Giannoglou G, Soulis J, Farmakis T, Papadopoulou S, Parcharidis G, Louridas G (2005) A computational model to predict aortic wall stresses in patients with systolic arterial hypertension. Med Hypotheses 65:1191–1195. https://doi.org/10.1016/j.mehy.2005.06.017

e Melo RG, Duarte GS, Lopes A, Alves M, Caldeira D, e Fernandes RF, Pedro LM (2022) Incidence and prevalence of thoracic aortic aneurysms: a systematic review and meta-analysis of population-based studies. Seminars Thoracic Cardiovasc Surg 34:1–16. https://doi.org/10.1053/j.semtcvs.2021.02.029

Guang Y, Cocciolone AJ, Crandall CL, Johnston BB, Setton LA, Wagenseil JE (2022) A multiphasic model for determination of water and solute transport across the arterial wall: effects of elastic fiber defects. Arch Appl Mech 92:447–459. https://doi.org/10.1007/s00419-021-01985-3

Gueldner PH, Darvish CJ, Chickanosky IKM, Ahlgren EE, Fortunato R, Chung TK, Rajagopal K, Benjamin CC, Maiti S, Rajagopal KR, Vorp DA (2024) Aortic tissue stiffness and tensile strength are correlated with density changes following proteolytic treatment. J Biomech 172:112226. https://doi.org/10.1016/j.jbiomech.2024.112226

Halabi CM, Broekelmann TJ, Lin M, Lee VS, Chu ML, Mecham RP (2017) Fibulin-4 is essential for maintaining arterial wall integrity in conduit but not muscular arteries. Sci Adv 3:e1602532. https://doi.org/10.1126/sciadv.1602532

Holmes MH, Mow VC (1990) The nonlinear characteristics of soft gels and hydrated connective tissues in ultrafiltration. J Biomech 23:1145–1156. https://doi.org/10.1016/0021-9290(90)90007-p

Hornstra IK, Birge S, Starcher B, Bailey AJ, Mecham RP, Shapiro SD (2003) Lysyl oxidase is required for vascular and diaphragmatic development in mice. J Biol Chem 278:14387–14393

Huang ZJ, Tarbell JM (1997) Numerical simulation of mass transfer in porous media of blood vessel walls. Am J Physiol 273:H464–H477. https://doi.org/10.1152/ajpheart.1997.273.1.H464

Hwang CW, Edelman ER (2002) Arterial ultrastructure influences transport of locally delivered drugs. Circ Res 90:826–832

Igoucheva O, Alexeev V, Halabi CM, Adams SM, Stoilov I, Sasaki T, Arita M, Donahue A, Mecham RP, Birk DE, Chu ML (2015) Fibulin-4 E57K knock-in mice recapitulate cutaneous, vascular and skeletal defects of recessive cutis laxa 1B with both elastic fiber and collagen fibril abnormalities. J Biol Chem 290:21443–21459. https://doi.org/10.1074/jbc.M115.640425

Isselbacher EM (2005) Thoracic and abdominal aortic aneurysms. Circulation 111:816–828. https://doi.org/10.1161/01.CIR.0000154569.08857.7A

Isselbacher EM, Preventza O, Hamilton Black J, 3rd, Augoustides JG, Beck AW, Bolen MA, Braverman AC, Bray BE, Brown-Zimmerman MM, Chen EP, Collins TJ, DeAnda Jr. A, Fanola CL, Girardi LN, Hicks CW, Hui DS, Schuyler Jones W, Kalahasti V, Kim KM, Milewicz DM, Oderich GS, Ogbechie L, Promes SB, Gyang Ross E, Schermerhorn ML, Singleton Times S, Tseng EE, Wang GJ, Woo YJ (2022) 2022 ACC/AHA guideline for the diagnosis and management of aortic disease: a report of the American Heart Association/American College of Cardiology Joint Committee on clinical practice guidelines. Circulation. https://doi.org/10.1161/CIR.0000000000001106

Kailash, K. A., J. Z. Hawes, A. J. Cocciolone, M. R. Bersi, R. P. Mecham, and J. E. Wagenseil (2024) Constitutive modeling of mouse arteries suggests changes in directional coupling and extracellular matrix remodeling that depend on artery type, age,

sex, and elastin amounts. J Biomech Eng 146. https://doi.org/10.1115/1.4063272
Kiani C, Chen L, Wu YJ, Yee AJ, Yang BB (2002) Structure and function of aggrecan. Cell Res 12:19–32. https://doi.org/10.1038/sj.cr.7290106
Lai WM, Hou JS, Mow VC (1991) A triphasic theory for the swelling and deformation behaviors of articular cartilage. J Biomech Eng 113:245–258. https://doi.org/10.1115/1.2894880
Levin AD, Vukmirovic N, Hwang CW, Edelman ER (2004) Specific binding to intracellular proteins determines arterial transport properties for rapamycin and paclitaxel. Proc Natl Acad Sci U S A 101:9463–9467. https://doi.org/10.1073/pnas.0400918101
Li Y, Ren P, Dawson A, Vasquez HG, Ageedi W, Zhang C, Luo W, Chen R, Li Y, Kim S, Lu HS, Cassis LA, Coselli JS, Daugherty A, Shen YH, LeMaire SA (2020) Single-cell transcriptome analysis reveals dynamic cell populations and differential gene expression patterns in control and aneurysmal human aortic tissue. Circulation 142:1374–1388. https://doi.org/10.1161/CIRCULATIONAHA.120.046528
Lin PK, Davis GE (2023) Extracellular matrix remodeling in vascular disease: defining its regulators and pathological influence. Arterioscler Thromb Vasc Biol 43:1599–1616. https://doi.org/10.1161/ATVBAHA.123.318237
Lovich MA, Philbrook M, Sawyer S, Weselcouch E, Edelman ER (1998) Arterial heparin deposition: role of diffusion, convection, and extravascular space. Am J Physiol 275:H2236–H2242. https://doi.org/10.1152/ajpheart.1998.275.6.H2236
Maas SA, Ellis BJ, Ateshian GA, Weiss JA (2012) FEBio: finite elements for biomechanics. J Biomech Eng 134. https://doi.org/10.1115/1.4005694
Maas SA, Herron M, Weiss JA, Ateshian GA (2024) FEBio user manual. https://help.febio.org/docs/FEBioUser-3-6/UM36-3.12.2.3.html. Accessed 4 July 2024
Meccanici, F., C. G. E. Thijssen, S. Dekker, L. R. Bons, A. L. Gokalp, Y. B. de Rijke, J. J. M. Takkenberg, M. M. Mokhles, J. A. Bekkers, E. Boersma, E. Bouwens, A. E. van der Bosch, R. R. L. van Kimmenade, and J. W. Roos-Hesselink (2023) Circulating biomarkers associated with aortic diameter in male and female patients with thoracic aortic disease: a cross-sectional study. Open Heart 10. https://doi.org/10.1136/openhrt-2023-002317
Michel JB, Jondeau G, Milewicz DM (2018) From genetics to response to injury: vascular smooth muscle cells in aneurysms and dissections of the ascending aorta. Cardiovasc Res 114:578–589. https://doi.org/10.1093/cvr/cvy006
Michel JB, Thaunat O, Houard X, Meilhac O, Caligiuri G, Nicoletti A (2007) Topological determinants and consequences of adventitial responses to arterial wall injury. Arterioscler Thromb Vasc Biol 27:1259–1268. https://doi.org/10.1161/ATVBAHA.106.137851
Miller, C. C. (1924) The Stokes Einstein law for diffusion in solution. In: Proceedings of the royal society of london series a-containing papers of a mathematical and physical character 106:724–49. https://doi.org/10.1098/rspa.1924.0100
Pereira L, Lee SY, Gayraud B, Andrikopoulos K, Shapiro SD, Bunton T, Biery NJ, Dietz HC, Sakai LY, Ramirez F (1999) Pathogenetic sequence for aneurysm revealed in mice underexpressing fibrillin-1. Proc Natl Acad Sci U S A 96:3819–3823
Piao C, Zhang W-M, Deng J, Zhou M, Liu T-T, Zheng S, Jia L-X, Song W-C, Liu Y, Jie Du (2024) Activation of the alternative complement pathway modulates inflammation in thoracic aortic aneurysm/dissection. Am J Physiol Cell Physiol 326:C647–C658. https://doi.org/10.1152/ajpcell.00210.2023
Rastogi V, Stefens SJM, Houwaart J, Verhagen HJM, de Bruin JL, van der Pluijm I, Essers J (2022) Molecular imaging of aortic aneurysm and its translational power for clinical risk assessment. Front Med (Lausanne) 9:814123. https://doi.org/10.3389/fmed.2022.814123
Roccabianca S, Bellini C, Humphrey JD (2014) Computational modelling suggests good, bad and ugly roles of glycosaminoglycans in arterial wall mechanics and mechanobiology. J R Soc Interface 11:20140397. https://doi.org/10.1098/rsif.2014.0397
Shirasu T, Koyama H, Miura Y, Hoshina K, Kataoka K, Watanabe T (2016) Nanoparticles effectively target rapamycin delivery to sites of experimental aortic aneurysm in rats. PLoS ONE 11:e0157813. https://doi.org/10.1371/journal.pone.0157813
Sugiyama K, Marzi J, Alber J, Brauchle EM, Ando M, Yamashiro Y, Ramkhelawon B, Schenke-Layland K, Yanagisawa H (2021) Raman microspectroscopy and Raman imaging reveal biomarkers specific for thoracic aortic aneurysms. Cell Rep Med 2:100261. https://doi.org/10.1016/j.xcrm.2021.100261
Sun, Y., K. Asano, L. Sedes, A. Cantalupo, J. Hansen, R. Iyengar, M. J. Walsh, and F. Ramirez (2023) Dissecting aortic aneurysm in Marfan syndrome is associated with losartan-sensitive transcriptomic modulation of aortic cells. JCI Insight 8. https://doi.org/10.1172/jci.insight.168793
Tada S, Tarbell JM (2004) Internal elastic lamina affects the distribution of macromolecules in the arterial wall: a computational study. Am J Physiol Heart Circ Physiol 287:H905–H913. https://doi.org/10.1152/ajpheart.00647.2003
Touat Z, Lepage L, Ollivier V, Nataf P, Hvass U, Labreuche J, Jandrot-Perrus M, Michel J-B, Jondeau G (2008) Dilation-dependent activation of platelets and prothrombin in human thoracic ascending aortic aneurysm. Arterioscler Thromb Vasc Biol 28:940–946. https://doi.org/10.1161/ATVBAHA.107.158576
Unal M, Akkus O (2018) Shortwave-infrared Raman spectroscopic classification of water fractions in articular cartilage ex vivo. J Biomed Opt 23:1–11. https://doi.org/10.1117/1.JBO.23.1.015008
Wagenseil JE, Nerurkar NL, Knutsen RH, Okamoto RJ, Li DY, Mecham RP (2005) Effects of elastin haploinsufficiency on the mechanical behavior of mouse arteries. Am J Physiol Heart Circ Physiol 289:H1209–H1217. https://doi.org/10.1152/ajpheart.00046.2005
Weiss D, Rego BV, Cavinato C, Li DS, Kawamura Y, Emuna N, Humphrey JD (2023) Effects of age, sex, and extracellular matrix integrity on aortic dilatation and rupture in a mouse model of marfan syndrome. Arterioscler Thromb Vasc Biol 43:e358–e372. https://doi.org/10.1161/ATVBAHA.123.319122
Wolinsky H, Glagov S (1967) A lamellar unit of aortic medial structure and function in mammals. Circ Res 20:99–111
Yanagisawa H, Wagenseil J (2020) Elastic fibers and biomechanics of the aorta: Insights from mouse studies. Matrix Biol 85–86:160–172. https://doi.org/10.1016/j.matbio.2019.03.001
Yang X, Xu C, Yao F, Ding Q, Liu H, Luo C, Wang D, Huang J, Li Z, Shen Y, Yang W, Li Z, Yu F, Fu Y, Wang L, Ma Q, Zhu J, Xu F, Cong X, Kong W (2023) Targeting endothelial tight junctions to predict and protect thoracic aortic aneurysm and dissection. Eur Heart J 44:1248–1261. https://doi.org/10.1093/eurheartj/ehac823
Yousef S, Matsumoto N, Dabe I, Mori M, Landry AB, Lee SR, Kawamura Y, Yang C, Li G, Assi R, Vallabhajosyula P, Geirsson A, Moeckel G, Humphrey JD, Tellides G (2021) Quantitative not qualitative histology differentiates aneurysmal from nondilated ascending aortas and reveals a net gain of medial components. Sci Rep 11:13185. https://doi.org/10.1038/s41598-021-92659-1